



LAWRENCE
LIVERMORE
NATIONAL
LABORATORY

Signal and Image Processing Research at the Lawrence Livermore National Laboratory

Randy S. Roberts, Lisa A. Poyneer, Laura M.
Kegelmeyer, Carmen J. Carrano, David H.
Chambers, James V. Candy

July 2, 2009

SPIE Optics and Photonics Information Processing III
San Diego, CA, United States
August 3, 2009 through August 6, 2009

Disclaimer

This document was prepared as an account of work sponsored by an agency of the United States government. Neither the United States government nor Lawrence Livermore National Security, LLC, nor any of their employees makes any warranty, expressed or implied, or assumes any legal liability or responsibility for the accuracy, completeness, or usefulness of any information, apparatus, product, or process disclosed, or represents that its use would not infringe privately owned rights. Reference herein to any specific commercial product, process, or service by trade name, trademark, manufacturer, or otherwise does not necessarily constitute or imply its endorsement, recommendation, or favoring by the United States government or Lawrence Livermore National Security, LLC. The views and opinions of authors expressed herein do not necessarily state or reflect those of the United States government or Lawrence Livermore National Security, LLC, and shall not be used for advertising or product endorsement purposes.

Signal and Image Processing Research at the Lawrence Livermore National Laboratory

Randy S. Roberts, Lisa A. Poyneer, Laura M. Kegelmeyer, Carmen J. Carrano,
David H. Chambers, and James V. Candy
{roberts38, poyneer1, kegelmeyer1, carrano2, chambers2, candy1}@llnl.gov

Lawrence Livermore National Laboratory,
Livermore, CA 94550 USA

ABSTRACT

Lawrence Livermore National Laboratory is a large, multidisciplinary institution that conducts fundamental and applied research in the physical sciences. Research programs at the Laboratory run the gamut from theoretical investigations, to modeling and simulation, to validation through experiment. Over the years, the Laboratory has developed a substantial research component in the areas of signal and image processing to support these activities. This paper surveys some of the current research in signal and image processing at the Laboratory. Of necessity, the paper does not delve deeply into any one research area, but an extensive citation list is provided for further study of the topics presented.

Keywords: Lawrence Livermore National Laboratory, Signal and Image Processing, Adaptive Optics, National Ignition Facility Optics Inspection, Speckle Imaging, Time Reversal Signal Processing, Radiation Detection and Isotope Identification

1. INTRODUCTION

Lawrence Livermore National Laboratory (LLNL) was founded in 1952 to conduct research on the design of thermonuclear weapons. Over the years, the Laboratory has evolved into an institution that conducts research in many different scientific and engineering disciplines. Since its inception, the Laboratory has built research programs around the three pillars of modern scientific inquiry: theoretical investigation, modeling and simulation, and validation through experiment. In the early years, signal and image processing played an important role in the design of instrumentation and evaluating experimental data related to weapons design. Today, this role continues with a focus on non-nuclear experimentation with the stockpile stewardship program. In addition, as the Laboratory expands its role into other areas such as energy research and nuclear non-proliferation activities, signal and image processing continued to grow as disciplines fundamental to many programs.

This paper describes some of the recent research activities in signal and image processing at LLNL. In particular, vignettes of recent advances in adaptive optics, optics inspection for the National Ignition Facility, speckle imaging, time-reversal signal processing, and radionuclide detection are presented. The paper does not provide depth on the selected topics. Rather, interested readers are referred to an extensive list of citations.

2. SOME RECENT RESEARCH AREAS

2.1 Signal processing for high precision control in Adaptive Optics

Research in Adaptive Optics (AO) began at the Laboratory in the mid-1990s. Research and development interests in this area include ophthalmological applications, and control systems for large telescopes.¹⁻¹⁶ Here we describe research on the control algorithms for the AO system of the Gemini

Planet Imager (GPI). This instrument is designed to image Jovian planets that are one to ten million times fainter than their parent stars, and adaptive optics is key to realizing this objective. Poyneer and her colleagues have recently made seminal advances in the area of high precision control of adaptive optics, and their techniques are slated to be implemented on GPI. Here we briefly discuss four advances: Fourier transform wavefront reconstruction, the spatially filtered wavefront sensor, Optimized-gain Fourier Control and Predictive Fourier Control. Together, these techniques enable direct imaging of extra-solar planets by improving AO performance well beyond present general purpose systems.

Most AO systems operate by conjugating the phase aberration of the wavefront. This perturbed wavefront is corrected through phase conjugation on the surface of a deformable mirror (DM). The corrected wavefront is then used by the system, i.e., it is imaged by a science camera. The DM is almost always controlled in a closed loop where the aberration of the wavefront is measured by a wavefront sensor (WFS). Because the derivative of the phase, not the phase itself, is usually measured, the true phase must be determined through the process of wavefront reconstruction. Given this residual phase, a control algorithm is used to determine the best shape for the DM to take to correct the temporally-varying phase aberration.

AO performance can be measured in terms of both the residual phase error and the quality of the point-spread function (PSF) of the imaging system. In astronomical applications, a well-functioning AO system can have a few hundred nanometers of residual error, which substantially sharpens the PSF and significantly improves imaging quality. A general-purpose AO system similar to those in current use is simulated in Fig. 1, (termed “Small, slow system” in the figure). (All PSFs are apodized to suppress diffraction.) Though the PSF has a defined core, when it is examined on a log-scale, there is a large halo of scattered light which prevents high contrast imaging. That said, GPI requires the AO system to have only a few tens of nanometers of residual error. A first key step to enable this performance is to design a system that operates at higher frame rates and with many more control points, termed actuators, on the DM. GPI’s design has ~ 1600 actuators, instead of a few hundred, and will run at frame rates up to 1.5 kHz. Higher rates allow the AO system to better adapt with the dynamic atmosphere; more actuators allow the DM to more accurately approximate the phase aberration’s spatial structure.

The primary barrier to faster and larger systems is the computational cost of the wavefront reconstruction. Traditional implementation of matrix-based wavefront reconstruction are too expensive. Poyneer, et. al., developed a computationally efficient Fourier Transform Reconstruction (FTR) technique. This technique treats the reconstruction problem as a filtering problem: the wavefront sensor can be described with a filter, and the reconstruction is simply the inverse filter, applied with Fourier transforms. Although reconstruction using Fourier Transforms had been previously considered using square periodic apertures, the FTR technique was designed for realistic (i.e. annular) apertures. Because of computationally efficient DFTs, FTR takes 45 times less computation per reconstruction than the traditional matrix multiplication for GPI. This enables GPI to be built with an off-the-shelf computer as the controller, instead of very expensive custom-programmed DSPs. In addition to being fast, FTR provides a flexible framework for sophisticated wavefront control strategies, as discussed later.

The PSF of a fast AO system with ~ 1600 actuators is shown in Fig. 1 (termed “Large, fast system”). FTR enables a square region of better correction to be formed around a tight core of the PSF. Outside this square region is the uncorrectable high spatial frequency phase aberrations caused by the atmosphere. Inside this square region is the correctable phase. Note that in this configuration performance is limited, as indicated by a “+” shape of scattered light inside the square. This shape is caused by aliasing in the wavefront sensor. Because the Shack-Hartmann WFS samples the phase, the measurements suffer from aliasing. High spatial frequency phase errors are incorrectly measured as low spatial frequency ones, leading to significant performance degradation in closed loop. One easy way to prevent aliasing is to low-pass filter the signal before sampling. This is done optically

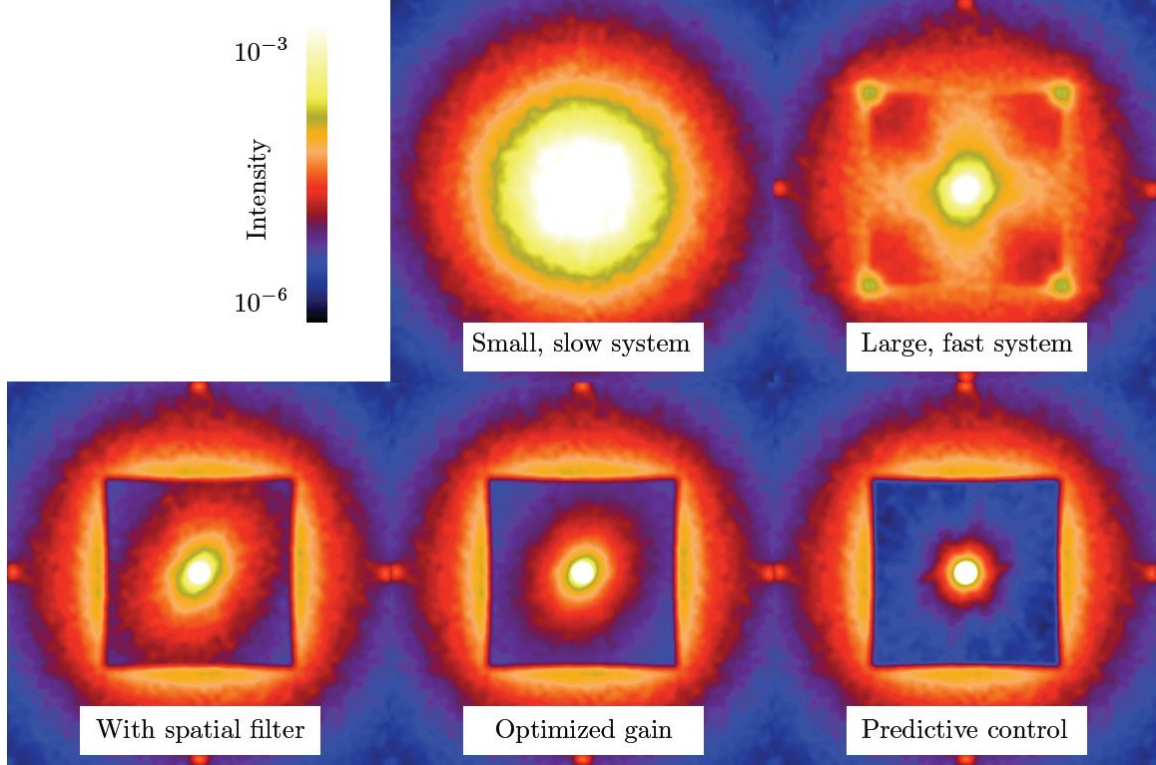


Figure 1: Five different 12-second point-spread functions (PSFs) for a 6th magnitude star and five-layer frozen flow atmosphere simulation. See the text for descriptions of the AO technique used in each simulation. From a general purpose AO system (“Small, slow system”) to the Gemini Planet Imager with prediction (“Predictive control”), there is 100 times less scattered light in the dark hole region where extra-solar planets will be imaged.

by the spatially filtered WFS with a square field stop.^{5,6} For typical GPI operating conditions, the spatial filter will attenuate high spatial frequency phase power by a factor of 1000, essentially removing the aliasing error term. This excellent attenuation of high spatial frequency phase prevents the aliasing error term that can dominate large, fast AO systems.

Spatially filtering the WFS greatly improves the performance of high-performance AO systems. The PSF (“With spatial filter” in Fig. 1) no longer has this “+” pattern of light. Instead a dark hole is generated, exposing the true performance of the closed-loop AO system. The remaining scattered light is due to residual atmospheric error (from temporal lags in the AO system) and WFS noise. Performance can be further improved through optimization of the system’s wavefront control algorithms. Such an optimization technique is used in matrix-based AO systems. Termed modal gain optimization, this method works by optimizing the gain of the integral controller for each mode given AO telemetry. Poyneer and Véran applied this technique to Fourier reconstruction, after determining that FTR provides independent control of each spatial frequency in the wavefront.¹ In this modal formulation, the optimized gains are implemented as a filter. Optimized-gain Fourier Control (OFC) provides several advantages over the existing matrix-based gain optimization methods. Again, using Fourier modes provides significant computational advantage in determining the new optimal control parameters and implementation that control. A particular advantage is that in the high-performance case the Fourier modes directly correspond to spatial locations in the PSF’s dark hole. As a result, (see “Optimized gain” in Fig. 1) minimizing the error on each Fourier mode minimizes the scattered light at all spatial locations in the dark hole. This optimization is particularly important because natural variations in atmospheric power and wind velocities cause the controllable Fourier modes

to have a wide range of optimal gains. Without this adaptive optimization to current operating conditions, GPI's AO system would have sub-optimal contrast at nearly all locations inside the dark hole.

In astronomical AO, layers of wind in the atmosphere can appear to blow turbulence across the aperture (a process termed frozen flow); this creates structure which a predictive controller could exploit. Because the Fourier modes are spatially and temporally uncorrelated under frozen flow, each Fourier mode can be predicted independently, allowing drastic reduction of the model complexity and computational cost. Furthermore, the temporal power spectrum of a Fourier mode has a compact and easily identifiable shape under frozen flow: each layer contributes to a narrow peak of power in temporal frequency. This means that specific atmospheric layers can be easily identified using closed-loop telemetry.

Using this insight, and building on the closed-loop Kalman model of Le Roux, Poyneer and her colleagues developed a state space model for AO prediction of a Fourier mode with an atmosphere composed of an arbitrary number of wind-blown layers.⁸ She derived a steady-state Kalman filter from this model and showed how closed-loop telemetry provides the parameters necessary to solve the Algebraic Riccati Equation and determine each mode's predictive controller. Furthermore, the Kalman filter is computationally efficient, and allows the measurement of atmospheric characteristics during operation.

This predictive controller is stable, computationally efficient and effective. All of the PSFs in Fig. 1 were generated with a simulated AO system correcting a five-layer atmosphere with frozen flow. When Predictive Fourier Control is used (see "Predictive control" PSF in the figure), these layers are easily detected and then predicted, resulting in a much darker and more uniform dark hole. For GPI, moderate wind-blown turbulence will produce substantial power in the 40-80 Hz range. This is why prediction is so useful: an integral controller does not correct that power well, even when optimized. The Kalman filter, on the other hand, can selectively correct each layer, even in this temporal frequency range.

2.2 National Ignition Facility Optics Inspection

The Laboratory has a long history with the development of lasers and their application to achieving ignition (controlled fusion). This past May 2009, the National Ignition Facility (NIF) was dedicated with its threefold mission: provide key experimental resources to ensure the safety and reliability of the national nuclear deterrent, enable breakthroughs in planetary science and astrophysics, and to study fusion as a potential energy source. NIF is the highest-energy laser system in the world, consisting of 192 laser beams that can be focused into a small volume, the size of a pencil eraser. When fully operational, NIF will be able to deliver two million joules of energy and create temperatures and pressures that exist in stars.

A key technology that enables NIF to deliver such energy is highly specialized optics technology and the continual inspection of those optics. It is critical to the operation of the laser system to detect and characterize imperfections in the optics thereby minimizing scattering and maximize energy throughput. Automated optics inspection allows NIF operators to monitor the optics trains in each of the 192 beam lines, and remove optics to mitigate imperfections or refurbish the optic as needed. Each beamline can contain dozens of optics, for a total of approximately eight thousand pieces in the aggregate system. The inspections are complicated in that they are performed *in situ* by imaging along the beam lines, through other optics and adjusting the focus to a particular optic. Various illumination techniques (backlighting, edgelighting, etc.) and focal lengths can be applied to individual optics to gather the necessary information for imperfection detection and characterization. As a result, imperfections in the optics can appear as dark regions on a bright background, or bright regions on a dark background. The resolution of the imagery is approximately 20 μm , readily enabling the detection of imperfections on the order of 50 μm . The number of pixels per image

ranges from 4096×4096 to 16384×16384 .

Kegelmeyer, et. al, have developed a comprehensive suite of image analysis and pattern recognition tools to detect, characterize and track imperfections in NIF optics.^{17,18} Imagery is preprocessed so that the background of the optic is dark, and imperfections in the optic appear bright. The imagery is next processed with the Local Area Signal-to-Noise Ratio (LASNR) image segmentation algorithm.¹⁷ LASNR has been found to be highly effective at detecting imperfections in NIF optics inspection imagery. Essentially, it estimates the signal-to-noise ratio for each pixel in an image, using a local-area neighborhood surrounding the pixel to estimate noise statistics. Several neighborhood sizes are selected using *a-priori* information on the anticipated sizes of the imperfections. Applying LASNR at several scales yields a family of local-area SNR images, one for each scale size. Applying preselected thresholds associated with each scale yields (at least) one seed pixel within each imperfection. (Computationally efficient methods have been developed to implement the multi-scale LASNR algorithm.) Seed pixels from different scales are combined, and the resulting seed pixel is used with an adaptive threshold to segment the imperfection from the background.

After imperfections have been detected and segmented from the background, a number of attributes of the imperfection are calculated. Examples include area in pixels, sum of pixel intensities, mean and standard deviation of pixel intensities, minimum, maximum of pixel intensities, long and short axis of the best-fit ellipse, edge strength, and similar features. Features extracted from imperfections are tracked over time to characterize the rate of change of the imperfection. Optical experts examine the features to determine when intervention is required. To aid the optics experts in this determination, a machine learning technology called Avatar is employed. Avatar is a suite of machine learning tools developed by Sandia National Laboratories (Albuquerque, New Mexico) (<http://www.ca.sandia.gov/avatar>) which are exceptional in that its parameters are self regulating for maximum accuracy. For example, it creates an ensemble of decision trees from training data such that the number of trees optimizes the out-of-bag accuracy. By carefully creating an accurate and extensive training set for use with Avatar, the NIF Optics Inspection output has greatly reduced the number of false alarms from an untenable number that could not be reviewed in many hours to a small number that can be reviewed in minutes.

2.3 Speckle Imaging

For many surveillance and target identification applications the imaging system must look through the atmosphere along a horizontal or slant path. Turbulence along the path causes variations in the index-of-refraction that lead to phase errors in the propagating field. When the optical beam is brought to focus the resulting image is blurred by the atmospheric phase errors. For a typical near-ground horizontal path the blurring can be quite severe. The resolution of an eight-inch telescope will be reduced by as much as a factor of 20 along a horizontal path in average atmospheric turbulence.

In a short exposure image looking through the atmosphere, the atmospheric phase errors are frozen in time. The image is a speckle pattern which contains spatial frequencies all the way out to the diffraction limit. No information is lost—it is just scrambled in phase. If the short exposure images are averaged, the resulting long exposure image is blurred, even if the imagery was stabilized. The high spatial frequencies are lost in the averaging process.

The Laboratory began to conduct research in speckle imaging in the early-1990s, and continues to this day.^{19–26} The imaging can be modeled as the convolution

$$i_n(\mathbf{x}) = \tau_n(\mathbf{x}) * \mathbf{o}(\mathbf{x}) \quad (1)$$

where $i_n(\mathbf{x})$ is the n^{th} speckle image in an ensemble, $\mathbf{o}(\mathbf{x})$ is the object, and $\tau_n(\mathbf{x})$ is the combined atmosphere-telescope point-spread function. Fourier transforming both sides of Eqn. 1, the Fourier

magnitude can be estimated by averaging the power spectrum over each frame:

$$|O(\mathbf{u})|^2 = \frac{\langle |\mathbf{I}_n(\mathbf{u})|^2 \rangle_n}{\langle |\tau_n(\mathbf{u})|^2 \rangle_n} \quad (2)$$

Since $\langle \tau_n(\mathbf{x}) \rangle$ is unknown, it is modeled using the Labeyrie-Korff transfer function where the atmosphere coherence length is iterated to find the best value. The complex bispectrum $I_{B,n}(\mathbf{u}, \mathbf{v})$ is used to find estimate the phase. It is defined as

$$I_{B,n}(\mathbf{u}, \mathbf{v}) = \mathbf{I}_n(\mathbf{u})\mathbf{I}_n(\mathbf{v})\mathbf{I}_n(-\mathbf{u} - \mathbf{v}) \quad (3)$$

where \mathbf{u} and \mathbf{v} are spatial frequency vectors. The Fourier phase of the object is recursively related to the phase of the average complex bispectrum according to a three point integration:

$$\arg |O(\mathbf{u} + \mathbf{v})| = \arg |\mathbf{O}(\mathbf{u})| + \arg |\mathbf{O}(\mathbf{v})| - \arg |\langle \mathbf{I}_{B,n}(\mathbf{u}, \mathbf{v}) \rangle_n| \quad (4)$$

The phase of the object is recovered through recursive application of Eqn. 4. After the Fourier magnitude and phase have been estimated, they are combined and inverse transformed to recover the image.

In the past few years Carrano and her colleagues have made several advances in speckle imaging.²¹⁻²⁶ To test initial concepts on enhanced surveillance, a prototype speckle imaging system was developed using commercially available components. One of the keys to this system is the availability of off-the-shelf high-resolution cameras with computer interfaces. The prototype system is based on an eight-inch Cassegrain telescope, a 1280x1024 pixel commercial video camera with an electronic shutter capable of < 1 ms exposures, and a laptop computer. The prototype system has been tested in a series of experiments conducted at standoff distances from 0.5 km to 60 km over a broad range of atmospheric and lighting conditions. The figures in Fig. 2 show examples of imagery acquired from the top of Mt Diablo, a 3849' peak in Northern California, located approximately 30 km from LLNL. In Fig. 2a and 2b the three objects in the image are cargo, water, and flatbed trucks imaged at a range of 29 km and in Fig. 2c and 2d we are looking at Lick observatory on the top of Mt. Hamilton. The speckle image reconstructions on the right provide significantly higher resolution than the unprocessed images on the left.

2.4 Time reversal techniques for characterizing targets and enhancing communications in complex environments

Over the last 15 years, there has been a rapid growth in applications of time-reversal symmetry of wave propagation to enhance communications and imaging in complex environments. These techniques exploit both temporal and spatial reciprocity of wave propagation to mitigate signal distortion created from the large number of independent propagation paths between a transmitter and receiver. Recent work has shown that time-reversal techniques can distinguish and locate targets in highly scattering environments. Work at the Laboratory has gone beyond imaging to show that time-reversal analysis of array data can reveal target characteristics such as size, shape, orientation, and composition.²⁷⁻³⁰

The application of time reversal symmetry to target characterization begins with the concept of a time reversal array (TRA). In acoustics this consists of an array of transducers that can record the pressure at each transducer location, store the resulting time series, reverses the series, then transmit the reversed signal back into the medium. If there is a source in the medium, the TRA will record the radiated field at the element locations, then transmit a reversed field that focuses back onto the source. This focusing occurs even when the medium is highly scattering with multiple propagation paths between source and array. If there is no source, the array focuses on the scatterer that reflects the most energy transmitted from the array. A TRA requires a way to record and digitize signals, save them in memory, then retransmit them. This is possible for most acoustic signals but becomes

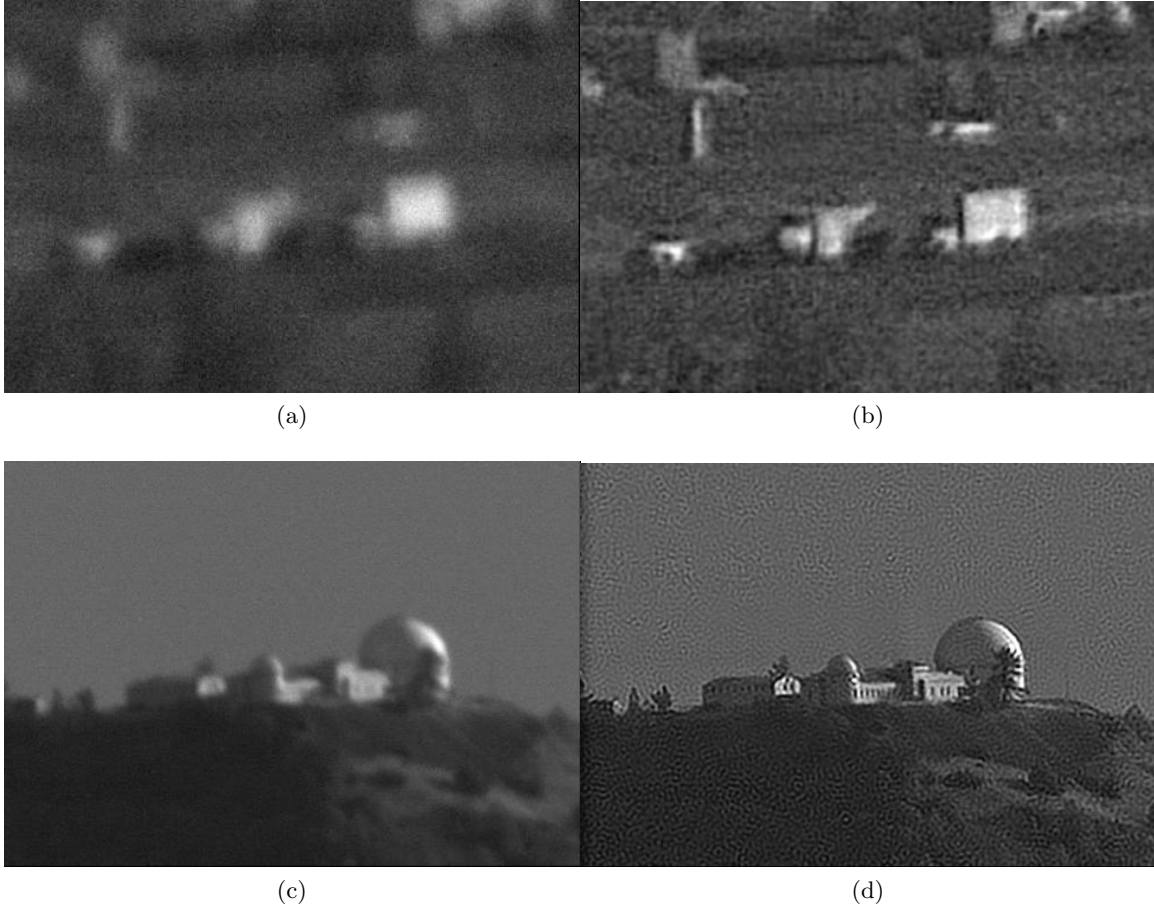


Figure 2: Two examples of speckle image processing. The top example was collected at a range of 29 km, and the bottom figure at 60km.

challenging at radar frequencies. Fortunately, there is another way to exploit the properties of time reversal using a more conventional multistatic array system.

Suppose we have an array of N transmitters and a separate array of M receivers. Let each transmit element emit a pulse and then record the received signals from each element of the receiver. The resulting M by N array of received signals is the *multistatic response matrix* (MRM) for the array system. This matrix constitutes the data collected by the array system and contains information about the medium and objects within the volume interrogated by the array. Processing for target characterization begins by taking the Fourier transform of the MRM. For each frequency we then calculate the singular value decomposition (SVD) to obtain a set of singular vectors and singular values. If $K(\omega)$ is the Fourier transformed MRM, the SVD is

$$\mathbf{K}(\omega) = \mathbf{U}(\omega)\mathbf{S}(\omega)\mathbf{V}^\dagger(\omega), \quad (5)$$

where \mathbf{S} is a diagonal matrix whose size is the rank of \mathbf{K} . \mathbf{U} is a matrix of M singular vectors associated with the receivers and \mathbf{V} is a matrix of N singular vectors associated with the transmitters. The advantage of using the SVD to decompose the MRM comes from the association between the singular values and the targets in the array field of view.³⁰ Each singular value represents a scattering mode for a target and the associated singular vectors can be used to focus the field onto the target.

Consider a simple case of a linear array of 21 elements and three targets (Fig. 3). The distribution of singular values of the MRM (Fig. 3b) can be divided into three large singular values and 18 smaller

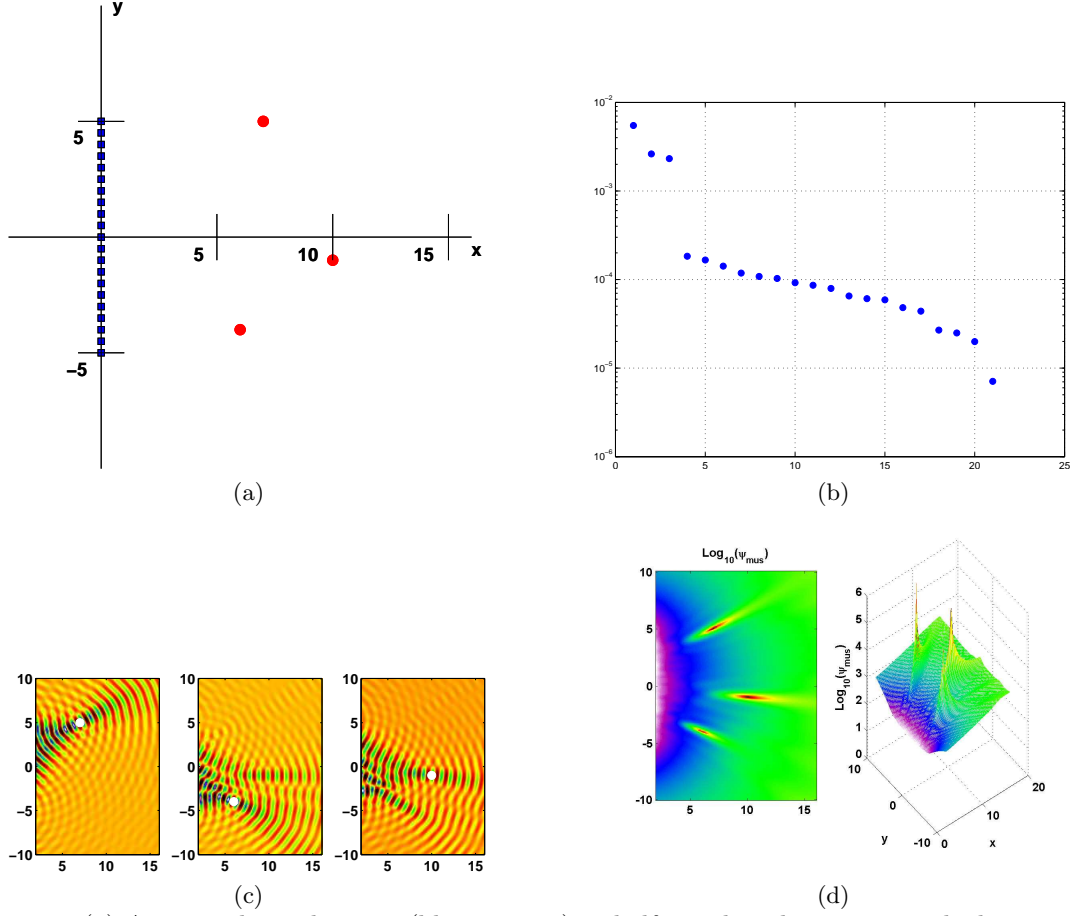


Figure 3: (a) Array with 21 elements (blue squares) at half wavelength spacing, with three targets (red dots) at x, y positions (10, -1), (6, -4), (7, 5) with strengths 2, 1, and 3 respectively. (b) Spectrum of singular values for array and targets in Fig. 3. Largest three singular values are associated with the targets. The remaining 18 are associated with noise. (c) Fields created by the three singular vectors associated with the targets (white dots) in Fig. 3b. Each field focuses on the target. (d) MUSIC functional for three targets, image and surface views.

values. The fields associated with the three largest singular values focus on the scatterers (Fig. 3c). Since the remaining 18 singular vectors are orthogonal to these "target" singular vectors, we can use this condition to construct new imaging functionals (*e.g.* MUSIC) that enhance the ability to locate the targets (Fig. 3d).

In the more general case, more than one singular value can be associated with a given target. The relative sizes of the singular values and their variation with array geometry can be used to extract more information about the target. Figure 4a shows a linear array of small crossed electric dipoles that can be rotated around the look direction. For a small ellipsoidal target there can be up to six singular values depending on the conductivity, shape, location, and orientation associated with the target. Figure 4b shows the variation of the three singular values associated with a perfectly conducting disk whose rotational axis is tilted 45 deg from the look direction. As the array rotates the singular values vary periodically, with the largest singular value attaining its maximum value when the array axis is in the same plane as the disk axis. This would allow one in principle to extract orientation information of nonsymmetric targets from the singular value distribution without creating an image of the target. Additional results can be found in the review paper by Chambers.³⁰

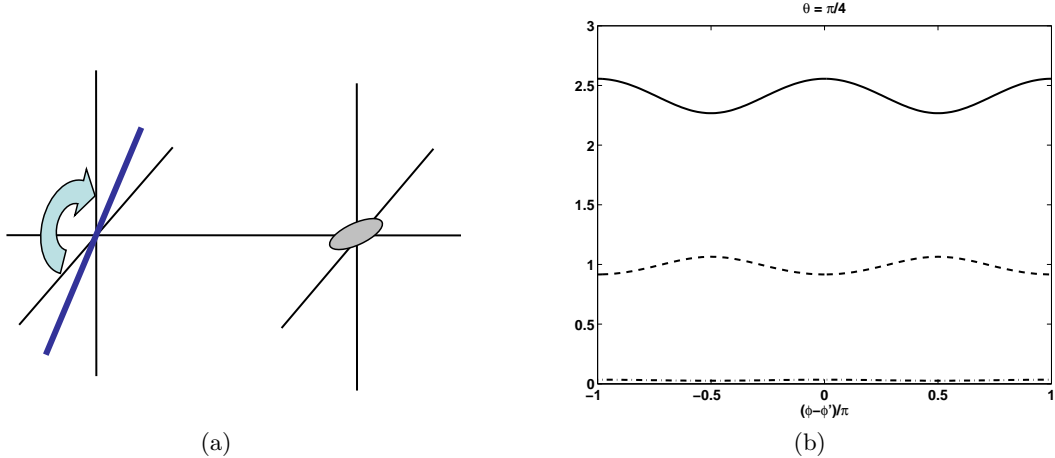


Figure 4: (a) Rotating linear array of small crossed dipole elements with an ellipsoid target. (b) Singular values 1 (solid), 2 (dashed), and 3 (dash-dot) for a rotating linear array of crossed dipoles and a perfectly conducting disk whose center axis is tilted 45 deg from the look direction. As the array rotates the singular values vary in a periodic pattern, with the largest singular value maximum when the array and the disk axis are in the same plane.

Time-reversal methods have also been applied to the problem of communication in a highly reverberant environment. The fundamental concept involves time-reversing the impulse response or Green's function characterizing the uncertain communications channel to mitigate dispersion and multi-path effects. Experiments with an acoustic communication system placed in a highly reverberant room show that these methods can significantly reduce the effects of multipath and noise for both narrow and wide band systems. Time-reversal methods can be applied in either a broadcast scenario where a signal is transmitted to all possible receivers, or in a stealth mode where only one receiver can receive the signal. Possible applications include battlefield communications, transmission through waveguides (ducts), underwater communications, and propagation of signals through highly scattering media (structures). Laboratory work in this area can be found in a series of papers by Candy *et al.*²⁷⁻²⁹

2.5 Bayesian Sequential Processing for Radionuclide Detection and Parameter Estimation

The Laboratory has a long history of research and development in radiation detection and isotope identification. Considerable effort has been put towards developing detectors, and algorithms to processed detector data.³¹⁻³³ Recently, Candy, et. al. have been investigating Bayesian approaches to the detection of radionuclides.³⁴ The goal of their work is to provide quick detection of radioactive contraband for low count data (ie., a small number of measurements) using sequential processing.

Radionuclides emit photons of characteristic energies at random times. These photons can be detected, and their energy converted into a pulse where the pulse height is proportional to the photon's energy. Traditionally, the pulses are binned by energy to form a histogram. The shape of the histogram (also called a pulse-height spectrum) is then used to detect the isotope(s) that produced the photons. The left hand side of Figure 5 illustrates a pulse-height spectrum. That figure plots energy(volts) versus count for a set of experimental composite radionuclide data consisting of three radionuclides: cobalt (^{60}Co), cesium (^{137}Cs), barium (^{133}Ba) with 2, 1 and 5 energy lines (monoenergetic sources), respectively.

Candy and his colleagues model the source radionuclides as a superposition (union) of monoenergetic (i.e., constant energy amplitude) sources. In this model, measured data consists of a low count, impulsive-like, time series of measurements (energy vs time) called an *event mode*

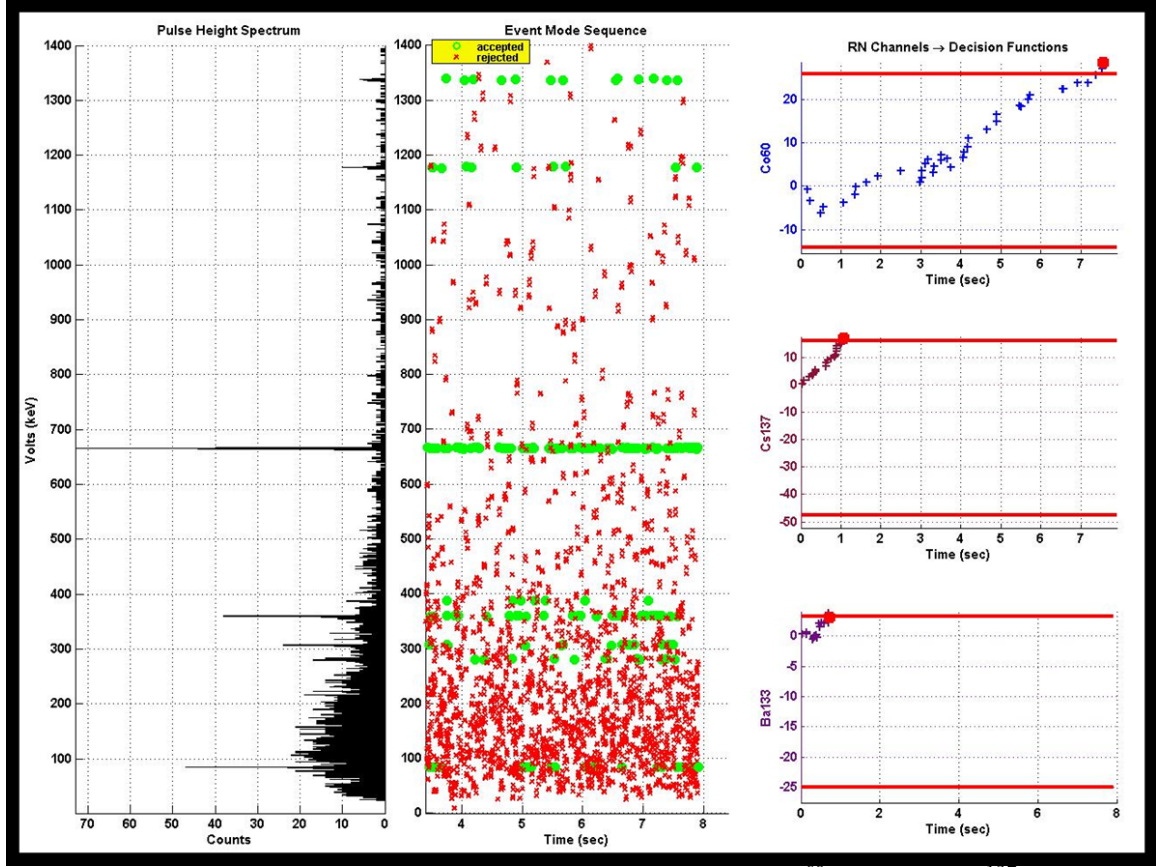


Figure 5: The plot on the left is a pulse-height spectrum of cobalt (^{60}Co), cesium (^{137}Cs), barium (^{133}Ba) with background. The center plot is the *event mode sequence* (EMS) of the data. The right column of plots is the processor output for the detection of (top to bottom) ^{60}Co , ^{137}Cs and ^{133}Ba , along with the detection threshold.

sequence (EMS). Define $\xi(n; \epsilon_m, \tau_m)$ as the component of an EMS sequence as the n^{th} -arrival from the m^{th} -monoenergetic source of *energy level* (amplitude), $\epsilon_m(n)$ and *arrival time*, $\tau_m(n)$ with associated *decay rate*, $\lambda_m(n)$ —as a single photon impulse sample, that is, $\xi(n; \epsilon_m, \tau_m) = \epsilon_m(n)\delta(t - \tau_m(n))$ and source rate $\lambda_m(n)$. In order to define the entire emission sequence over a specified time interval, $[t_o, T)$, we introduce the set notation, $\tilde{\tau}_m := \{ \tau_m(1) \cdots \tau_m(N_\epsilon(m)) \}$ at the n^{th} -arrival with $N_\epsilon(m)$ the total number of *counts* for the m^{th} -source in the interval. Therefore, $\xi(n; \epsilon_m, \tilde{\tau}_m)$ results in a unequally-spaced impulse train. The *interarrival* time is defined by $\Delta\tau_m(n) = \tau_m(n) - \tau_m(n-1)$ for $\Delta\tau_m(0) = t_o$ with the corresponding set definition (above) of $\Delta\tilde{\tau}_m(n)$. Thus, from the detector measurement of the individual photon arrivals, or equivalently the entire EMS, a particular radionuclide can be uniquely characterized. It follows that a complete radionuclide can be represented in terms of its monoenergetic decomposition, that is, the EMS is:

$$\begin{aligned} \mathcal{R}_\eta(n; \underline{\epsilon}, \underline{\Delta\tau}) &= \sum_{m=1}^{M_\epsilon} \sum_{n=1}^{N_\epsilon(m)} \xi(n; \epsilon_m(n), \Delta\tau_m(n)) = \\ &= \sum_{m=1}^{M_\epsilon} \sum_{n=1}^{N_\epsilon(m)} \epsilon_m(n)\delta(t - \Delta\tau_m(n)) \end{aligned} \quad (6)$$

where $\mathcal{R}_\eta(n; \underline{\epsilon}, \underline{\Delta\tau})$ is the composite EMS of the radionuclide, M_ϵ is the number of monoenergetic source components in the composite EMS, $N_\epsilon(m)$ is the number (counts) of arrivals from the m^{th} -

monoenergetic source component in the time-interval, $[t_o, T)$, $\epsilon_m(n)$ is the n^{th} -arrival of γ -ray energy (amplitude) level of the m^{th} -monoenergetic component in the time-interval of the composite *EMS*, $\Delta\tau_m(n)$ is the n^{th} interarrival time of the m^{th} -monoenergetic component, in the time interval of the composite *EMS*. This representation can be extended even further to capture a set of radionuclides as well. Thus, this unique physics-based representation provides the basis to develop signal models for subsequent processing.

The underlying physics of photon production from radionuclides requires a slight modification to Equation 6. The emission of monoenergetic photons follows a well-defined probability structure, that is, *all* monoenergetic photons are *not* present in the *EMS* during an individual event (single photon arrival) only *one* of the energy amplitude levels is present as dictated by its branching or probability of occurrence (α_i) associated with its inherent structure as specified in its energy decay diagram. Therefore, we model this decay structure by a Markov chain model incorporating an *indicator function* $\mathcal{I}_j(m) = \delta_{jm}$ where δ_{jm} a Kronecker delta. Indicator function $\mathcal{I}_j(m)$ is a random variable such that $\Pr(\mathcal{I}_j(m) = 1 | \xi(n; \underline{\epsilon}, \underline{\tau})) = \Pr(\mathcal{I}_j(m) = 1 | \Xi_n) = \alpha_j$ for α_j the corresponding branching or *probability of occurrence* of the j^{th} -monoenergetic RN component conditioned on the set of *EMS* measurements $\Xi_n := \{\xi(1), \dots, \xi(n)\}$.

With the inclusion of branching probabilities, the monoenergetic radionuclide model thus becomes

$$\mathcal{R}_\eta(n; \underline{\epsilon}, \underline{\Delta\tau}) = \sum_{m=1}^{M_\epsilon} \sum_{n=1}^{N_\epsilon(m)} \mathcal{I}_j(m) \epsilon_m(n) \delta(t - \Delta\tau_m(n)) \quad (7)$$

With this in mind, the required radionuclide posterior distribution can be decomposed in terms of each arrival pair $(\epsilon_j(n), \Delta\tau_j(n))$ along with its associated probability of occurrence, α_j , that is,

$$\Pr(\mathcal{R}_\eta(n; \underline{\epsilon}, \underline{\Delta\tau}) | \Xi_n) = \Pr(\underline{\epsilon}(n), \underline{\Delta\tau}(n), \mathcal{I}_j(m) | \Xi_n) \quad (8)$$

Applying Bayes' rule we obtain

$$\begin{aligned} \Pr(\mathcal{R}_\eta(n; \underline{\epsilon}, \underline{\Delta\tau}) | \Xi_n) &= \Pr(\underline{\Delta\tau}(n) | \underline{\epsilon}(n), \mathcal{I}_j(m), \Xi_n) \\ &\times \Pr(\underline{\epsilon}(n) | \mathcal{I}_j(m), \Xi_n) \times \Pr(\mathcal{I}_j(m) | \Xi_n) \end{aligned} \quad (9)$$

The *posterior radionuclide probability* can be estimated photon-by-photon and therefore evolves to the following processor:

1. Given the “truth”: $[\{\alpha_m^t\}, \{\epsilon_m^t\}, \{\Delta\tau_m^t\}]; m = 1, \dots, M_\epsilon$ (from Tables);
2. Determine the j^{th} -monoenergetic component with $\Pr(\mathcal{I}_j(m) = 1) = \alpha_j$, *decide* on energy-interarrival pair $(\epsilon_j, \Delta\tau_j)$;
3. Given $m = j$ and the data Ξ_n , estimate the *energy amplitude distribution*: $\hat{\Pr}(\epsilon_j(n) | \Xi_n)$;
4. Given $\epsilon_j(n)$ and the data Ξ_n , estimate the *interarrival distribution*: $\hat{\Pr}(\Delta\tau_j(n) | \epsilon_j(n), \Xi_n)$;
5. Update the radionuclide posterior distribution $\Pr(\mathcal{R}_\eta(n; \epsilon_j, \Delta\tau_j) | \Xi_n)$ using Eq. 9; and
6. Decide if this estimated distribution “matches” the target radionuclide distribution.

The output of a processor implementing the above approach is illustrated in the plots on the right of Fig. 5. The plots illustrate that the detection of ^{137}Cs and ^{133}Ba within one second, and the detection of ^{60}Co within eight seconds. Observe that the rapid detection of these radionuclides illustrates the potential of Bayesian sequential processing for radionuclide detection.

2.6 Other Areas of Research

There are many other areas of research in signal and image processing at the Laboratory. Space limitations preclude even cursory discussion here, and interested readers are referred to the references. The Laboratory has a large effort in Non-Destructive Evaluation (NDE), with extensive radiography, computed tomography, and ultrasound facilities. Research in signal and image processing for NDE has been an ongoing effort for the past two decades. Some results from this area are found in the papers by Martz and his colleagues.^{35–41}

Video processing and exploitation have recently become important research areas for the Laboratory. Efforts in this area include image stabilization and registration,⁴² object and vehicle tracking.^{?,43–45} Video processing also plays an important role in NIF where it is used to determine the position of the laser beams for close loop alignment of the 192 beams. See the papers by Awwal and Wilhemsen for details.^{46–48} More generally, some recent results in recognizing objects in imagery can be found in the papers by Manay and Pagleroni.^{49,50}

3. CENTER FOR ADVANCES SIGNAL AND IMAGING SCIENCES

The Center for Advanced Signal and Imaging Sciences (CASIS) was founded by Jim Candy in the early 1990s with the purpose of providing a forum for Laboratory engineers and scientists to exchange technical information in the areas of signal and image processing. CASIS sponsors a two-day workshop each Fall, where researchers present their latest results. The workshop also has one or more keynote speakers that present their recent research to the Laboratory. Table 1 lists several past years of speakers and their topics. In recent years, the CASIS workshop has expanded its focus areas to include pattern analysis and machine intelligence, subjects that are of interest to signal and image processing researchers. The workshop has also expanded beyond the Laboratory to include technical staff from the neighboring Sandia National Laboratory.

| Year | Speaker | Title |
|------|----------------------------------|---|
| 2008 | Prof Jose Principe, U Florida | Information Theoretic Signal Processing |
| 2007 | Prof Jittendra Malik, Berkeley | Recognizing Objects and Actions in Images and Video |
| 2006 | Prof Sanjit Mitra, USC | Recent Research Results in Image and Video Processing |
| 2006 | Dr. James Candy, UCSB, LLNL | A Bayesian Approach to Nonlinear Statistical Signal Processing |
| 2005 | Prof James Flanagan, Rutgers | Natural Interfaces for Information Systems |
| 2004 | Proj James McClellan, GA Tech | Array Signal Processing for Locating Buried Objects and Tracking Moving Targets |
| 2004 | Prof Alan Oppenheim, MIT | Things My Mother Never Told Me (About Signal Processing) |
| 2003 | Dr. Thomas Budinger, Berkeley | Recent Advances in Medical Imaging |
| 2002 | Dr. Leon Cohen, U New York | Time-Frequency Descriptions of Signals |
| 2002 | Dr. Alan Witten, U. Oklahoma | Expedition Adventure using Geophysics to find Dinosaur Pirate Ships and Cavemen |
| 2001 | Prof. A. Paulraj, Stanford | Multiple Input Multiple Output (MIMO) Wireless: The New Frontier |
| 2001 | Dr. James Greenleaf, Mayo Clinic | Vibro-acoustography: Ultrasonic imaging without speckle |

Table 1: Recent CASIS speakers

4. SUMMARY

Signal and image processing are important technologies at the Lawrence Livermore National Laboratory. Although originally applied to analyzing nuclear weapons test data, they have emerged as independent research areas. Vignettes of several recent research and development efforts were presented, along with a long list of references. The Center for Advance Signal and Imaging Sciences was briefly described, along with a listing of recent keynote speakers.

5. ACKNOWLEDGMENTS

The authors would like to acknowledge the the Directorate of Engineering at the Lawrence Livermore National Laboratory for its sustained support of signal and image processing research and development at the Laboratory.

This work performed under the auspices of the U.S. Department of Energy by Lawrence Livermore National Laboratory under Contract DE-AC52-07NA27344.

REFERENCES

1. L. A. Poyneer, M. A. van Dam, and J.-P. Véran. Experimental verification of the frozen flow atmospheric turbulence assumption with use of astronomical adaptive optics telemetry. *J. Opt. Soc. Am.*, 26:833–846, 2009.
2. L. A. Poyneer, B. Bauman, B. A. Macintosh, D. Dillon, and S. Severson. Experimental demonstration of phase correction with a 32 x 32 microelectricalmechanical systems mirror and a spatially filtered wavefront sensor. *Opt. Lett.*, 31:293–295, 2006.
3. L. A. Poyneer and D. Dillon. MEMS Adaptive Optics for the Gemini Planet Imager: control methods and validation. *Proc. SPIE* **6888**, page 68880H, 2008.
4. L. A. Poyneer, D. Dillon, S. Thomas, and B. A. Macintosh. Laboratory demonstration of accurate and efficient nanometer-level wavefront control for extreme adaptive optics. *Appl. Opt.*, 47:1317–1326, 2008.
5. L. A. Poyneer and B. Macintosh. Adaptive optics: Spatially filtered wave-front sensor for high-order adaptive optics. *Optics & Photonics News*, 15(12):15, 2004.
6. L. A. Poyneer and B. Macintosh. Spatially filtered wave-front sensor for high-order adaptive optics. *J. Opt. Soc. Am. A*, 21:810–819, 2004.
7. L. A. Poyneer and Bruce A. Macintosh. Optimal Fourier Control performance and speckle behavior in high-contrast imaging with adaptive optics. *Opt. Exp.*, 14:7499–7514, 2006.
8. L. A. Poyneer, Bruce A. Macintosh, and Jean-Pierre Véran. Fourier transform wavefront control with adaptive prediction of the atmosphere. *J. Opt. Soc. Am. A*, 24:2645–2660, 2007.
9. L. A. Poyneer, D. W. Palmer, K. N. LaFortune, and B. Bauman. Experimental results for correlation-based wavefront sensing. *Proc. SPIE* **5894**, page 58940N, 2005.
10. L. A. Poyneer, M. Troy, B. Macintosh, and D. Gavel. Experimental validation of Fourier transform wave-front reconstruction at the Palomar Observatory. *Opt. Lett.*, 28:798–800, 2003.
11. L. A. Poyneer and J.-P. Véran. Towards feasible and effective predictive wavefront control for adaptive optics. *Proc. SPIE* **7015**, page 70151E, 2008.
12. L. A. Poyneer and J.-P. Véran. Predictive wavefront control for adaptive optics with arbitrary control loop delays. *J. Opt. Soc. Am. A*, 25:1486–1496, 2008.
13. L. A. Poyneer and J.-P. Véran. Adaptive wavefront calibration and control for the Gemini Planet Imager. In *Adaptive Optics: Analysis and Methods Topical Meeting on CD-ROM*, page AWB1, 2007.
14. L. A. Poyneer and J.-P. Véran. Efficient, adaptive wave-front control for high-order adaptive optics. In *Adaptive Optics: Analysis and Methods Topical Meeting on CD-ROM*, page AThA2, 2005.

15. L. A. Poyneer and J.-P. Véran. Optimal modal Fourier transform wave-front control. *J. Opt. Soc. Am. A*, 22:1515–1526, 2005.
16. L. A. Poyneer, J.-P. Véran, D. Dillon, S. Severson, and B. A. Macintosh. Wavefront control for the Gemini Planet Imager. *Proc. SPIE* **6272**, page 62721N, 2006.
17. L. M. Kegelmeyer, P. Fong, S. M. Glenn, and J. Liebman. Local area signal-to-noise ratio (lasnr) algorithm for image segmentation. In *SPIE: Applications of Digital Image Processing XXX (OP312, 6696-85)*, August 2007.
18. B.Y. Chen, L. M. Kegelmeyer, J. A. Liebman, J. T. Salmon, J. Tzeng, and D. W. Paglieroni. Detection of laser optic defects using gradient direction matching. In *SPIE - 8th International Conference on Laser Beam Control and Applications*, volume 6101, Jan 2006.
19. T. W. Lawrence, D. M. Goodman, E. M. Johanasson, and J. P. Fitch. Speckle imaging of satellites at the u. s. air force maui optical station. *Applied Optics*, 31:6307–6321, 1992.
20. S. G. Gibbard, B. Macintosh, and D. Gavel. Titan: High-resolution speckle images from the keck telescope. *Icarus*, 139:189–201, 1999.
21. C. Carrano. Mitigating atmospheric effects in high-resolution infra-red surveillance imagery with bispectral speckle imaging. In *Proc SPIE*, volume 6316, 2006.
22. C. Carrano. Adapting high-resolution speckle imaging to moving targets and platforms. In *Proc. SPIE*, volume 5409, 2004.
23. C. Carrano. Anisoplanatic performance of horizontal-path speckle imaging. In *Proc. SPIE*, volume 5162, 2003.
24. C. Carrano. Progress in horizontal and slant path imaging using speckle imaging. In *Proc. SPIE*, volume 5001, 2003.
25. C. Carrano. Horizontal and slant path surveillance with speckle imaging. In *AMOS Technical Conference proceedings*, page 499, 2002.
26. C. Carrano. Speckle imaging over horizontal paths. In *Proc SPIE*, volume 4825, page 109, 2002.
27. J. V. Candy, A. W. Meyer, A. J. Poggio, and B. L. Guidry. Time-reversal processing for an acoustic communications experiment in a highly reverberant environment. *J. Acoust. Soc. Am.*, 115:1621–1631, 2004.
28. J. V. Candy, A. J. Poggio, D. H. Chambers, B. L. Guidry, C. L. Robbins, and C. A. Kent. Multichannel time-reversal processing for acoustic communications in a highly reverberant environment. *J. Acoust. Soc. Am.*, 118:2339–2354, 2005.
29. J. V. Candy, D. H. Chambers, C. L. Robbins, B. L. Guidry, A. J. Poggio, F. Dowla, and C. A. Hertzog. Wideband multichannel time-reversal processing for acoustic communications in highly reverberant environments. *J. Acoust. Soc. Am.*, 120:838–851, 2006.
30. D. H. Chambers. Target characterization using time-reversal symmetry of wave propagation. *Int. J. Mod. Phys. B*, 21:3511–3555, 2007.
31. S E Labov, L Pleasance, P Sokkappa, W Craig, G Chapline, J Frank, M ; Gronberg, J G Jernigan, J Johnson, S ; Kammeraad, D Lange, A Meyer, K Nelson, B Pohl, D Wright, and R Wurtz. Foundations for improvements to passive detection systems-final report. Technical Report UCRL-TR-207129, Lawrence Livermore National Laboratory, Livermore,CA, Feb 2004.
32. K Nelson and P Sokkappa. Statistical model for generating a population of unclassified objects and radiation signatures spanning nuclear threats. Technical Report LLNL-TR-408407, Lawrence Livermore National Laboratory, 2008.
33. K E Nelson, T B Gosnell, and D A Knapp. The effect of gamma-ray detector energy resolution on the ability to identify radioactive sources. Technical Report LLNL-TR-411374, Lawrence Livermore National Laboratory, May 2009.
34. J. V. Candy, E. Breidfeller, B. Guidry, D. Manatt, K. Sale, D. Chambers, M. Axelrod, and A. Meyer. Physics-based detection of radioactive contraband: A sequential bayesian approach. In *IEEE OCEANS '09 Proceedings*, 2009.

35. Harry E. Martz Jr. and Daniel J. Schneberk. *Advanced Signal Processing Handbook: Theory and Implementation for Radar, Sonar and Medical Imaging Real-Time Systems*, chapter Industrial Computed Tomographic Imaging. CRC Press, Boca Raton, 2001.
36. Daniel J. Schneberk and Harry E. Martz. *Nondestructive Testing Handbook, third edition: Volume 4, Radiographic Testing*, volume Nondestructive Testing Handbook, third edition: Volume 4, Radiographic Testing, chapter Image Data Analysis. American Society for Nondestructive Testing, Columbus, OH, 2002.
37. William D. Brown and Jr. Harry E. Martz. X-ray digital radiography and computed tomography of icf and hedp materials, subassemblies and targets. In *Digital Imaging IX, An ASNT Topical Conference*, 2006.
38. E. J. Kokko, H. E. Martz, D. J. Chinn, H. R. Childs, J. A. Jackson, D. H. Chambers, D. J. Schneberk, and G. A. Clark. As-built modeling of objects for performance assessment. *J. Comp. Inf. Sci. Eng.*, 6(4):405–417, 2006.
39. Sain JD, Brown WB, Chinn DJ, Martz HE Jr, Morales KE, Schneberk DJ, and Updike EO. X-ray digital radiography and computed tomography characterization of targets. In *Eighteenth Target Fabrication Meeting*, May 2008.
40. Brown WB, Martz HE Jr, Bono MJ, Sain JD, and Teslich NE. X-ray digital radiography and computed tomography characterization of double-shell hedp targets. In *Seventeenth Target Fabrication Meeting*, October 2006.
41. Brown WB, Martz HE Jr., Sain JD, and Morales K. X-ray nondestructive characterization of mesoscale (mm extent with μm features) objects. In *Sixteenth Target Fabrication Specialists Meeting*, May 2005.
42. Mark Duchaineau, Jonathan Cohen, and Sheila Vaidya. Toward fast computation of dense image correspondence on the gpu. In *Proceedings of HPEC 2007, High Performance Embedded Computing, Eleventh Annual Workshop, Lincoln Laboratory, Massachusetts Institute of Technology*, pages 91–92, 18-20 Sept, 2007.
43. C. Carrano. Mtrack 2.0: An ultra-scale tracking algorithm for low-resolution overhead imagery. Technical Report LLNL-TR-410382, Lawrence Livermore National Laboratory, Feb 2009.
44. C. Carrano. Mtrack 1.0: A multi-vehicle, deterministic tracking algorithm. Technical Report LLNL-TR-404638, Lawrence Livermore National Laboratory, June 2008.
45. S. Samson, C. Cheung, and C. Kamath. Robust background subtraction with foreground validation for urban traffic video. *Eurasip Journal on applied signal processing*, 14:2330–2340, 2005.
46. C. Kamath, A. Gezahegne, S. Newsam, and G.M. Roberts. Salient points for tracking moving objects in video. In 5685, editor, *Proceedings, Image and Video Communications and Processing*. SPIE, January 2005.
47. K.C. Wilhelmsen, A. A. S. Awwal, S. W. Ferguson, B. Horowitz, V. J. Miller Kamm, and C. A. Reynolds. Automatic alignment system for the national ignition facility. In *Conference on Accelerator and Large Experimental Physics Control Systems*, Knoxville, TN, Oct 14-20 2007.
48. A. A. S. Awwal, K. L. Rice, and T. M. Taha. Fast implementation of matched filter-based automatic alignment image processing. *Optics and Laser Technology*, 41:193–197, Mar 2008.
49. A. A. S. Awwal, Wilbert A. McClay, Walter S. Ferguson, James V. Candy, Thad Salmon, and Paul Wegner. Detection and tracking of the back-reflection of kdp images in the presence or absence of a phase mask. *Applied Optics*, 45:3038–3048, 2006.
50. S. Manay and D. Paglieroni. Matching flexible polygons to fields of corners extracted from images. In *Proc. Int. Conf. on Image Analysis and Recog.*, August 22-24, 2007.
51. S. Manay and D. Paglieroni. Detecting polygons of variable dimension in overhead images with particle filters. In *Proc. IEEE Int. Conf. Image Proc.*, 12-15 Oct. 2008,.